

Mapping the ionized gas of the metal-poor H II galaxy PHL 293B with MEGARA

C. Kehrig,¹★† J. Iglesias-Páramo,^{1,2}★ J. M. Vílchez,¹★ A. Gil de Paz,^{3,4}★ S. Duarte Puertas,¹
E. Pérez-Montero,¹ A. I. Díaz,⁵ J. Gallego,^{3,4} E. Carrasco,⁶ N. Cardiel,^{3,4} M. L. García-Vargas,⁷
A. Castillo-Morales,^{3,4} R. Cedazo,⁸ P. Gómez-Álvarez,⁷ I. Martínez-Delgado,⁷ S. Pascual^{3,4}
and A. Pérez-Calpena⁷

¹Instituto de Astrofísica de Andalucía, CSIC, Apartado de correos 3004, E-18080 Granada, Spain

²Estación Experimental de Zonas Áridas (CSIC), Ctra. de Sacramento s/n, E-04120 Almería, Spain

³Departamento de Física de la Tierra y Astrofísica, Fac. CC. Físicas, Universidad Complutense de Madrid, Plaza de las Ciencias 1, E-28040 Madrid, Spain

⁴Instituto de Física de Partículas y del Cosmos IPARCOS, Fac. CC Físicas, Universidad Complutense de Madrid, Plaza de las Ciencias, 1, E-28040 Madrid, Spain

⁵Departamento de Física Teórica, Universidad Autónoma de Madrid, E-28049 Madrid, Spain

⁶Departamento Nacional de Astrofísica, Óptica y Electrónica, INAOE, Calle Luis Enrique Erro No.1, C.P. 72840 Tonantzintla, Puebla, Mexico

⁷FRONTAL, S.L.N.E., Calle Tulipán 2, portal 13, 1A, E-28231 Las Rozas de Madrid, Spain

⁸Universidad Politécnica de Madrid, 28031 Madrid, Spain

Accepted 2020 July 28. Received 2020 July 23; in original form 2020 April 24

ABSTRACT

Here we report the first spatially resolved spectroscopic study for the galaxy PHL 293B using the high-resolution GTC/MEGARA integral field unit (IFU). PHL 293B is a local, extremely metal-poor, high ionization galaxy. This makes PHL 293B an excellent analogue for galaxies in the early Universe. The MEGARA aperture (~ 12.5 arcsec \times 11.3 arcsec) covers the entire PHL 293B main body and its far-reaching ionized gas. We created and discussed maps of all relevant emission lines, line ratios, and physical–chemical properties of the ionized ISM. The narrow emission gas appears to be ionized mainly by massive stars according to the observed diagnostic line ratios, regardless of the position across the MEGARA aperture. We detected low intensity broad emission components and blueshifted absorptions in the Balmer lines ($H\alpha$, $H\beta$) which are located in the brightest zone of the galaxy ISM. A chemical homogeneity, across hundreds of parsecs, is observed in O/H. We take the oxygen abundance $12+\log(\text{O}/\text{H}) = 7.64 \pm 0.06$ derived from the PHL 293B integrated spectrum as the representative metallicity for the galaxy. Our IFU data reveal for the first time that the nebular He II $\lambda 4686$ emission from PHL 293B is spatially extended and coincident with the ionizing stellar cluster, and allow us to compute its absolute He II ionizing photon flux. Wolf-Rayet bumps are not detected excluding therefore Wolf-Rayet stars as the main He II excitation source. The origin of the nebular He II $\lambda 4686$ is discussed.

Key words: HeII regions – galaxies: dwarf – galaxies: individual: PHL 293B – galaxies: ISM – galaxies: starburst.

1 INTRODUCTION

H II galaxies are the most metal-poor starbursts in the local Universe (e.g. Westera et al. 2004; Kehrig et al. 2006; Izotov, Thuan & Guseva 2012; James et al. 2017). These galaxies present intense star-formation rates, and they usually have low masses and blue optical colours. The hot, luminous massive stars present in H II galaxies give off vast quantities of high-energy UV photons which ionize the gas producing strong nebular emission-line spectra (e.g. Kehrig, Telles & Cuisinier 2004; Cairós et al. 2009, 2010).

PHL 293B is a very compact H II galaxy (effective radius of its star-forming component ~ 0.7 arcsec; e.g. Papaderos et al. 2008) which belongs to the ‘Palomar–Haro–Luyten’ survey of faint galaxies (see French 1980; Kinman & Davidson 1981). The ionized gas of

PHL 293B presents a very low oxygen abundance of $12+\log(\text{O}/\text{H}) \approx 7.6$ –7.7 [$\sim 1/10$ solar metallicity¹; e.g. French (1980), Kinman & Davidson (1981), Papaderos et al. (2008), Izotov et al. (2011), Fernández et al. (2018)]. Moreover, PHL 293B shows ultrahigh excited gas indicated by the presense of the nebular H II $\lambda 4686$ emission (e.g. French 1980; Izotov, Thuan & Guseva 2007), and its very high specific star formation rate ($\text{sSFR} = \text{SFR}/M_\star \sim 6 \text{ Gyr}^{-1}$; see table 4 from Filho et al. 2013) is comparable to those found in the high-redshift Universe (e.g. Stark 2016). These features are more commonly observed and predicted in distant star-forming galaxies in comparison with local starburst (e.g. Lehnert et al. 2015; Mainali et al. 2018; Izotov, Thuan & Guseva 2019; Sobral et al. 2019). This makes PHL 293B a remarkable place nearby that allows us to study in detail physical conditions which may be predominant in primeval starbursts (see also Kehrig et al. 2016; Guseva et al.

* E-mail: kehrig@iaa.es (CK); jgilesia@iaa.es (JI-P); jvm@iaa.es (JMV); agil@fis.ucm.es (AGDP)

† Severo Ochoa IAA Fellow

¹ Assuming a solar abundance $12+\log(\text{O}/\text{H})_\odot = 8.69$ (Asplund et al. 2009)

Table 1. General properties of PHL 293B.

| Parameter | PHL 293B |
|--------------------|------------------------|
| Alternate names | Kinman Dwarf, A2228-00 |
| R.A. (J2000.0) | 22h 30m 36.8s |
| DEC. (J2000.0) | −00° 06′ 37″ |
| redshift | 0.0051 |
| D^a (Mpc) | 23.1 |
| HType ^b | Im? |
| Scale (pc/arcsec) | 112 |
| $(B-V)^c$ | 0.56 ± 0.05 |
| $(V-R)^c$ | 0.27 ± 0.04 |
| M_B^c (mag) | −14.37 |
| A_V^d (mag) | 0.193 |

Note. ^aDistance taken from the NASA/IPAC Extragalactic Database (NED);

^bHubble Type from NED; ^cFrom Cairós et al. (2001); ^dGalactic extinction from Schlafly & Finkbeiner (2011)

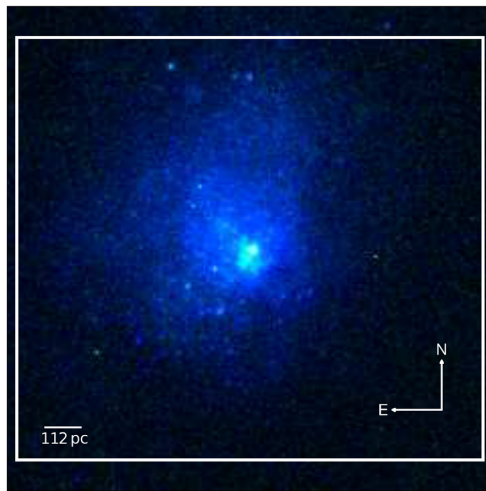


Figure 1. Colour composite *HST* image of PHL 293B generated using the following bands: blue = WFC3/F606W, green = WFC3/438W, red = WFC3/F814W (*HST* Proposal ID 12018; PI: A.Prestwich). The white box denotes the observed field of view (FOV) of MEGARA ($12.5 \text{ arcsec} \times 11.3 \text{ arcsec}$). North is up and east is to the left.

2017; Izotov et al. 2018; Kehrig et al. 2018; Senchyna et al. 2019). The optical spectrum of PHL 293B shows the typical strong narrow emission lines normally seen in the spectra of H II galaxies. Besides, its spectrum exhibits other features as low-intensity broad wings and blueshifted narrow absorptions in the hydrogen recombination lines (e.g. Izotov & Thuan 2009; Terlevich et al. 2014, and references therein). Table 1 lists other general properties of PHL 293B. Fig. 1 shows a three-colour composite image of PHL 293B from the *Hubble Space Telescope* (*HST*)/WFC3 which reveals an extended gaseous nebulae and star-forming activity mainly present in the southern zone of the galaxy (see also Papaderos et al. 2008).

In the last years, spatially resolved spectroscopy has opened a new window on to our understanding of the ionized gas in low-redshift SF galaxies, preventing us from an oversimplified view of it (e.g. Kehrig et al. 2008, 2013; Duarte Puertas et al. 2019; Sánchez 2020; Ucci et al. 2019). In this work, we present the first 2D spectroscopic study of PHL 293B based on commissioning observations with the *Multi Espectrógrafo en GTC de Alta Resolución para Astronomía* (MEGARA; see the next section). Our MEGARA data provide a detailed scanning of the structure and properties of the PHL 293B

ionized gas. Moreover, we derive the first integrated spectrum and total He II-ionizing photon flux from PHL 293B.

The paper is organized as follows. In Section 2, we report observations and data reduction. Flux measurements and emission line intensity maps are presented in Section 3. In Section 4, we show the 2D view of the ionization structure and nebular properties. In Section 5, we present the integrated properties from selected regions of PHL 293B. Section 6 discusses the spatially resolved He II $\lambda 4686$ -emitting region and the origin of the He II excitation. Finally, Section 7 summarizes the main conclusions derived from this work.

2 OBSERVATIONS AND DATA REDUCTION

The data of PHL 293B were obtained with MEGARA (see Carrasco et al. 2018; Gil de Paz et al. 2018), attached to the 10.4 m GTC telescope at the Roque de los Muchachos Observatory. Observations were taken during the second commissioning run in 2017 July 25 and 29, using the Large Compact Bundle (LCB) IFU mode which provides a field of view (FOV) of $12.5 \times 11.3 \text{ arcsec}^2$ ($\sim 1.4 \text{ kpc} \times 1.3 \text{ kpc}$ at the distance of 23.1 Mpc; see Fig. 1), with a spaxel² diameter of 0.62 arcsec. In order to cover the main optical emission lines, the observations were carried out with three gratings; we used the ‘blue’ VPH405-LR (centred at 4025 Å) and ‘green’ VPH480-LB (centred at 4785 Å) gratings which give spectral ranges (Å)/dispersions (Å pix^{−1}) of $\sim 3653\text{--}4386/0.17$ and $\sim 4332\text{--}5196/0.20$, respectively. On the red side, the VPH665-HR (centred at 6602 Å) was utilized, providing a spectral range from $\sim 6445\text{--}6837$ and 0.09 Å pix^{-1} . The resolving power of the gratings are ~ 6000 in case of LR VPHs and $\sim 20\,000$ for VPH665-HR.

We observed a total of 2.25 h on the galaxy, with the integration time split into three exposures for each VPH: $3 \times 600 \text{ s}$ for VPH665-HR and VPH480-LR each, and $3 \times 1500 \text{ s}$ for VPH405-LR. The seeing was about 1 arcsec and 0.5 arcsec during the first and second observing nights, respectively. All science frames were observed at airmasses $\lesssim 1.2$ to minimize the effects due to differential atmospheric refraction. Additionally, all necessary calibration frames (exposures of arc lamps and of continuum lamps) were obtained.

The data reduction and sky subtraction were carried out using the MEGARA Pipeline as described in Pascual et al. (2019). Due to severe haze throughout the observing run, we did not flux-calibrate the data using standard stars. Instead, we flux-calibrated our spectra using the Sloan Digital Sky Survey (SDSS) spectrum of PHL 293B. First, we co-added the spaxels within a 3 arcsec-diameter aperture (i.e. the same size of the SDSS fibre), centred at the brightest spaxel of the LCB IFU, to create a 1D spectrum called the ‘SDSS-like’ MEGARA spectrum. We then measured the flux of the emission lines present in both the SDSS and SDSS-like MEGARA spectra. We compared these flux measurements by performing a third-order logarithm polynomial fit to obtain the sensitivity function which was applied to the science frames. Given that the SDSS spectrum (spectral range $\sim 3800\text{--}9000 \text{ Å}$) of PHL 293B does not cover our bluest emission lines [OII] $\lambda\lambda 3727, 3729 \text{ Å}$, the sensitivity function was extrapolated to allow for their relative flux calibration.

²Individual elements of IFUs are usually named ‘spatial pixels’ (so-called ‘spaxel’); the term is used to distinguish a spatial element on the IFU from a detector pixel.

3 FLUX MEASUREMENTS AND EMISSION LINE INTENSITY MAPS

Here we measure emission line fluxes from individual spaxels based on our own IDL scripts. On top of a linear flat continuum, we fit a Gaussian profile to each emission line using the IDL based routine MPFIT (Markwardt 2009); the peak intensity, the line width σ , and the central wavelength λ_C for each line are kept as free parameters. Note that, due to the high spectral resolution of MEGARA we were able to resolve the [O II] doublet and, consequently, measure its individual lines at $\lambda 3726 \text{ \AA}$ and $\lambda 3729 \text{ \AA}$. In the case of the $H\alpha + [N II]$ lines, we perform a simultaneous fit keeping a nitrogen $[N II]\lambda 6584/[N II]\lambda 6548$ line ratio of 3. Previous work, based on single-aperture/long-slit spectroscopy of the central star-forming (SF) knot of PHL 293B have detected the presense of several components for the $H\alpha$, $H\beta$ lines (e.g. Izotov & Thuan 2009; Terlevich et al. 2014; Fernández et al. 2018). Following these authors, we fit these Balmer lines assuming three Gaussian components: narrow + broad emission, and one absorption component. Errors in the derived parameters (line flux, peak intensity, line width σ , central wavelength λ_C) are estimated by using the bootstrap method.

By combining the line fluxes with the position of the spaxels on the sky, we create all maps presented in this paper. Fig. 2 exposes the intensity maps for several emission lines; only fluxes with $S/N > 3$ are displayed.³ We show for the first time the spatial distribution for the broad $H\alpha$, $H\beta$ components for PHL 293B. The global spatial structure of the brightest lines (narrow $H\beta$, [O III] $\lambda 5007$, and narrow $H\alpha$) is similar, with [O III] $\lambda 5007$ and narrow $H\alpha$ emission covering almost the entire FOV. The spatial distribution of the fainter lines (e.g. [O III] $\lambda 4363$, He II $\lambda 4686$, [N II] $\lambda 6584$, [S II] $\lambda 6717+6731$), and the broad $H\beta$ and $H\alpha$ are restricted to the inner parts of the galaxy.

When comparing the [O II] emission distribution to that for other relatively bright lines as $H\beta$, we find the former to be more compact. This could be related partially to the fact that the [O II] lines lie at the blue edge of the spectra (i.e. $\lambda < 3750 \text{ \AA}$) where we not only observe lower S/N but also expect less accuracy of the flux calibration (see Section 2 for details; see e.g. Sánchez et al. 2012; Yan et al. 2016; López-Sanjuan et al. 2019). However, we highlight that the PHL 293B ionization structure which seems to be dominated by high excitation should also play an important role; e.g. the [O III] $\lambda 5007$ emission is spatially wide-ranging as long as the [O II] $\lambda 3726, 3729$, [N II] $\lambda 6584$, and [S II] $\lambda 6717, 6731$ lines extend over a much smaller area (see Fig. 2). The likeness between the maps of [O II], [N II], and [S II] is generally expected due to their similar ionization potential, albeit [N II] and [S II] lines sit at the red part of the spectra where S/N and flux calibration effects mentioned above should be minor.

The emission of both, the high and low intensity lines, are peaked on the southern H II region where the star formation is mostly concentrated (the bright blue knot in Fig. 1; see also Papaderos et al. 2008). In agreement with previous work (e.g. Izotov & Thuan 2009; Terlevich et al. 2014) we were able to detect $H\beta$ and $H\alpha$ P Cygni-like profiles in some integrated spectra (see Section 5 for details) and in a few individual spaxels which are indicated in the map of the $H\beta$ and $H\alpha$ broad emission components (see Fig. 2). P Cygni-like profiles are displayed in Figs 3 and 4.

³ Here the S/N is defined as the ratio between the peak intensity of the emission line and the standard deviation of its underlying continuum.

4 SPATIALLY RESOLVED PROPERTIES OF THE IONIZED GAS

4.1 Ionization structure

Baldwin–Phillips–Terlevich (BPT) diagrams (Baldwin, Phillips & Terlevich 1981) are a powerful tool, widely used to separate star-forming galaxies and AGN. The spatially resolved BPT diagrams for PHL 293B are shown in Fig. 5: [O III] $\lambda 5007/H\beta$ versus [N II] $\lambda 6584/H\alpha$, [S II] $\lambda \lambda 6717, 6731/H\alpha$. These line ratios are not corrected for extinction, but reddening effects must be minor since these ratios involve lines which are close in wavelength. Each circle plotted in Fig. 5 corresponds to a line ratio obtained from a single spaxel, where the red circles show the He II $\lambda 4686$ -emitting spaxels. Based on stellar population synthesis and photoionization models, Kewley et al. (2001) proposed a theoretical demarcation curve that isolates galaxies with line ratios which are due to excitation by massive stars within H II regions from those where other ionizing source is needed. An empirical curve that differentiates between AGNs and H II-like systems was later derived by Kauffmann et al. (2003); both demarcation lines are plotted in Fig. 5. For all positions in PHL 293B our emission-line ratios fall in the general locus of SF objects, i.e. below and to the left of the separation lines in the two BPT diagrams. This suggests that photoionization from hot massive stars appears to be the dominant excitation mechanism within PHL 293B.

The spatial distribution for the BPT line ratios are displayed in Fig. 6. While highest and lowest values of [O III] $\lambda 5007/H\beta$ are found at the most inner and external zones of PHL 293B, respectively, a reverse trend is observed in the [N II] $\lambda 6584/H\alpha$ and [S II] $\lambda \lambda 6717, 6731/H\alpha$ maps, indicating the presense of higher excited gas inward. The [O III] $\lambda 5007/H\beta$ map clearly shows larger values spatially coincident with the southern H II region (i.e. the bright blue knot in Fig. 1) which also comprises the He II zone (see also the He II $\lambda 4686$ map in Fig. 2). Additionally, in Fig. 5 we see that the He II-emitting spaxels tend to have higher [O III] $\lambda 5007/H\beta$ ratio in comparison to the other spaxels. Shall we note that despite this correlation, the hard He II-ionizing radiation ($E \gtrsim 4 \text{ Ryd}$) does not have to be necessarily the main responsible for the brighter [O III] emission since the [O III] lines can be excited by softer energies ($E \gtrsim 2.5 \text{ Ryd}$) (see e.g. Thuan & Izotov 2005).

4.2 Nebular physical–chemical properties on a spaxel-by-spaxel basis

We have used the expressions from Pérez-Montero (2017) to compute the physical properties and ionic abundances of the PHL 293B ionized gaseous nebulae. These expressions are derived from the PyNEB tool (Luridiana, Morisset & Shaw 2015).

In Fig. 7 we show the maps for the [O II] $\lambda 3729/\lambda 3726$ and [S II] $\lambda 6717/\lambda 6731$ line ratios which are good indicators of the average electron density (n_e) in a nebula (Osterbrock & Ferland 2006). For most of the spectra, the observed [O II] ([S II]) line ratios correspond to n_e values $\lesssim 300 \text{ cm}^{-3}$ ($\lesssim 100 \text{ cm}^{-3}$), indicating a relatively low-density ionized gas in the central parts of PHL 293B.

For the [O III] $\lambda 4363$ -emitting spaxels, we have computed the electron temperature $T_e[\text{O III}]$ values from the reddening corrected [O III] $\lambda 4363/[\text{O III}]\lambda 5007$ line ratio. We have measured the weak [O III] $\lambda 4363$ line above 3σ for 29 spaxels which extend to an area of around 9.6 arcsec^2 equivalent to 0.12 kpc^2 (see Fig. 2). The top-left-hand panel of Fig. 8 presents the map of the $T_e[\text{O III}]$ which reveals values going from $\gtrsim 14000 \text{ K}$ to near 20000 K , with a

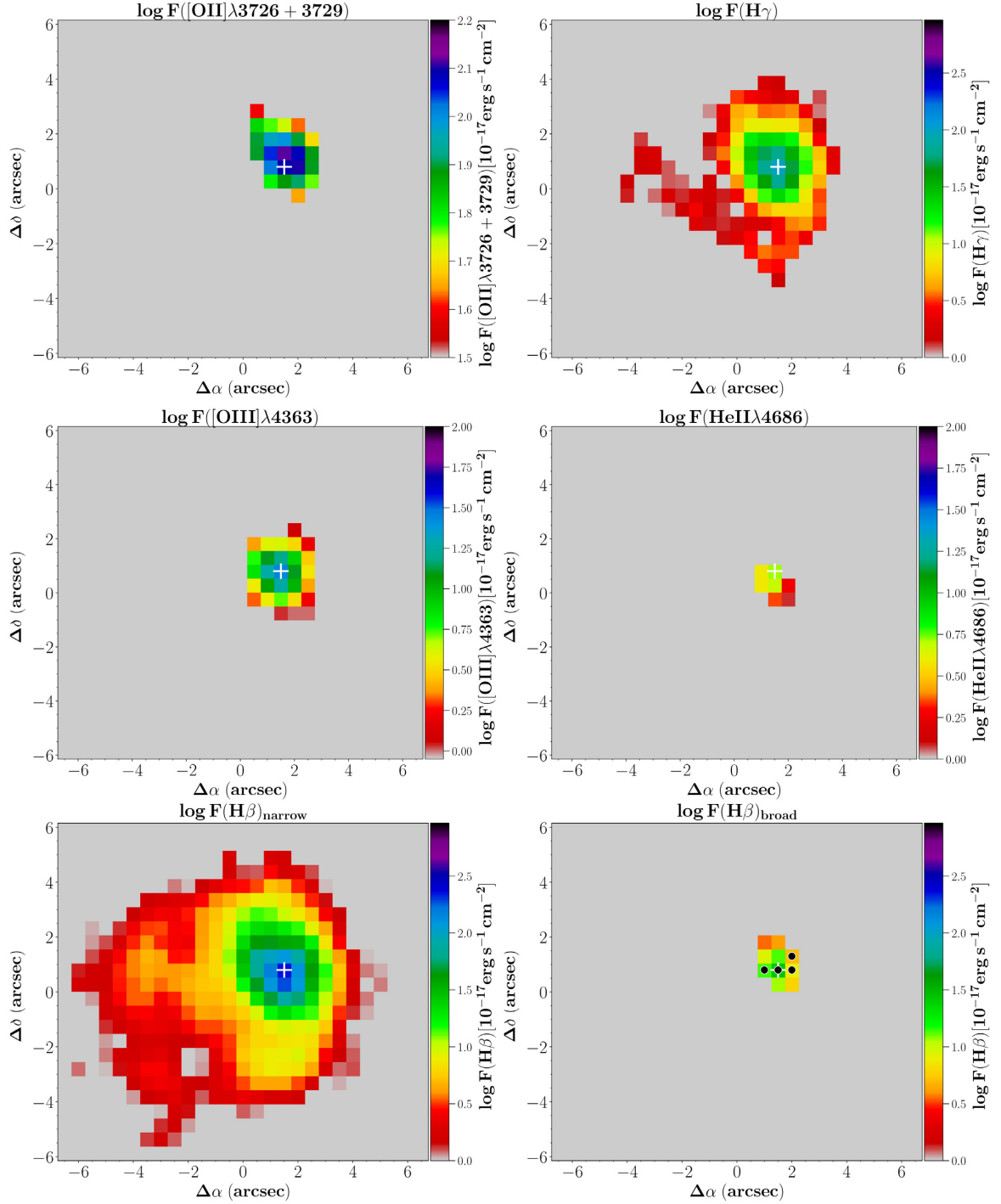


Figure 2. Flux maps in logarithmic scale. Only fluxes with $S/N > 3$ are shown. East is left and North is up. The plus (+) sign indicating the $H\alpha$ emission peak is plotted for orientation. The spaxels with no measurements available are left grey. The spaxels where we detect a P Cygni-like profile in the $H\beta$ line are indicated with a black circle on the map for the $H\beta$ broad emission. The spaxel where we detect a P Cygni-like profile in the $H\alpha$ line is indicated with a red circle on the $H\alpha$ broad emission map; this spaxel corresponds to the $H\alpha$ emission peak. The black continuous line in the $H\alpha$ narrow emission map demarcates the brightest area of the galaxy enclosing only spaxels with $H\alpha$ S/N (per pixel) > 100 (see Section 5 for details).

good fraction of the points clustering around the average T_e value of $\sim 18\,300$ K. The relation between $T_e[\text{O III}]$ and the S/N measured for the $[\text{O III}]\lambda 4363$ line is plotted in the bottom panel of Fig. 8 where no systematic effects are observed. This is an evidence that the largest values of $T_e[\text{O III}]$ that we derive are not an effect of overestimated $[\text{O III}]\lambda 4363$ flux measurements. We have used the $T_e[\text{O II}] - T_e[\text{O III}]$

empirical relationship from Pilyugin et al. (2006) to determine the $T_e[\text{O II}]$ values since no low-excitation auroral line (e.g. $[\text{N II}]\lambda 5755$) has been detected in any spaxel.

The O^+/H^+ and O^{2+}/H^+ ionic abundance ratios were computed from the $[\text{O II}]\lambda 3726, 29$ and $[\text{O III}]\lambda 5007$ lines, respectively, using the corresponding electron temperatures. A tiny fraction of the unseen

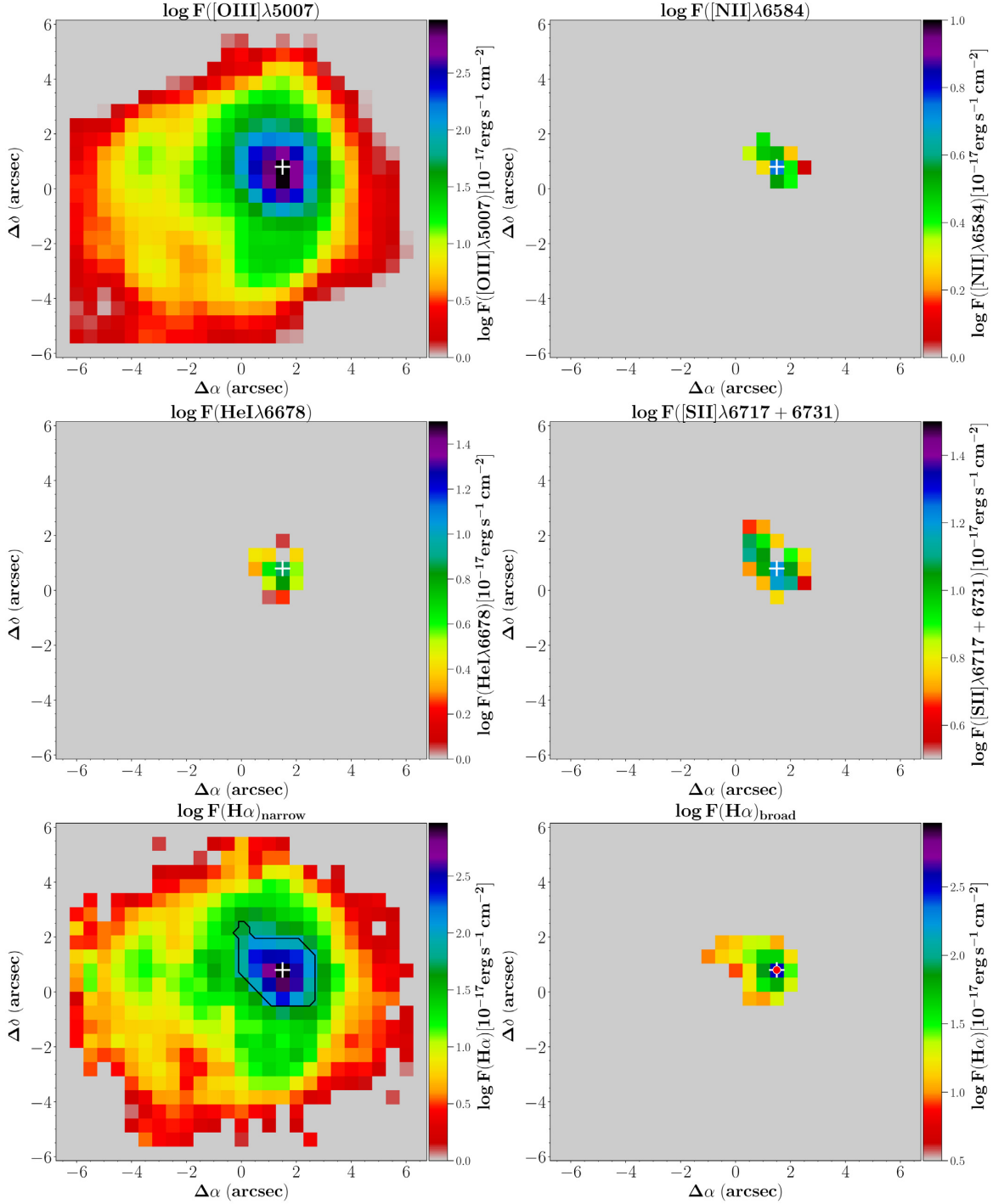


Figure 2 – continued

O^{3+} ion is expected to be present in high-ionizing SF regions as the ones showing He II emission. Based on the photoionization models from Izotov et al. (2006a), the O^{3+}/O^+ ratio is > 1 per cent only in the highest excitation H II regions whose $\text{O}^+/(\text{O}^+ + \text{O}^{2+})$ is lower than 10 per cent. We have checked that for all [O III] $\lambda 4363$ -emitting spaxels (including non-He II $\lambda 4686$ and He II $\lambda 4686$ emitting spaxels), $\text{O}^+/(\text{O}^+ + \text{O}^{2+})$ is $\gtrsim 10$ per cent; therefore the total O/H is assumed to be $\text{O}^+/\text{H}^+ + \text{O}^{2+}/\text{H}^+$. The spatial distribution of the derived $12+\log(\text{O}/\text{H})$ is displayed in the top-right-hand panel of Fig. 8 with

most of the spaxels (80 per cent) showing oxygen abundance in the range of ≈ 7.5 – 7.6 . Our results, thus, indicate that the warm gas-phase O/H in PHL 293B stands largely constant beyond hundreds of parsecs. This agrees with the absence of significant abundance gradient commonly observed in the ionized gas of H II galaxies (e.g. Kobulnicky & Skillman 1996; Izotov et al. 1999; Thuan, Izotov & Foltz 1999; Izotov, Chaffee & Green 2001; Izotov et al. 2004, 2006b; Papaderos et al. 2006; Kehrig et al. 2008, 2013, 2016; Pérez-Montero et al. 2009, 2011).

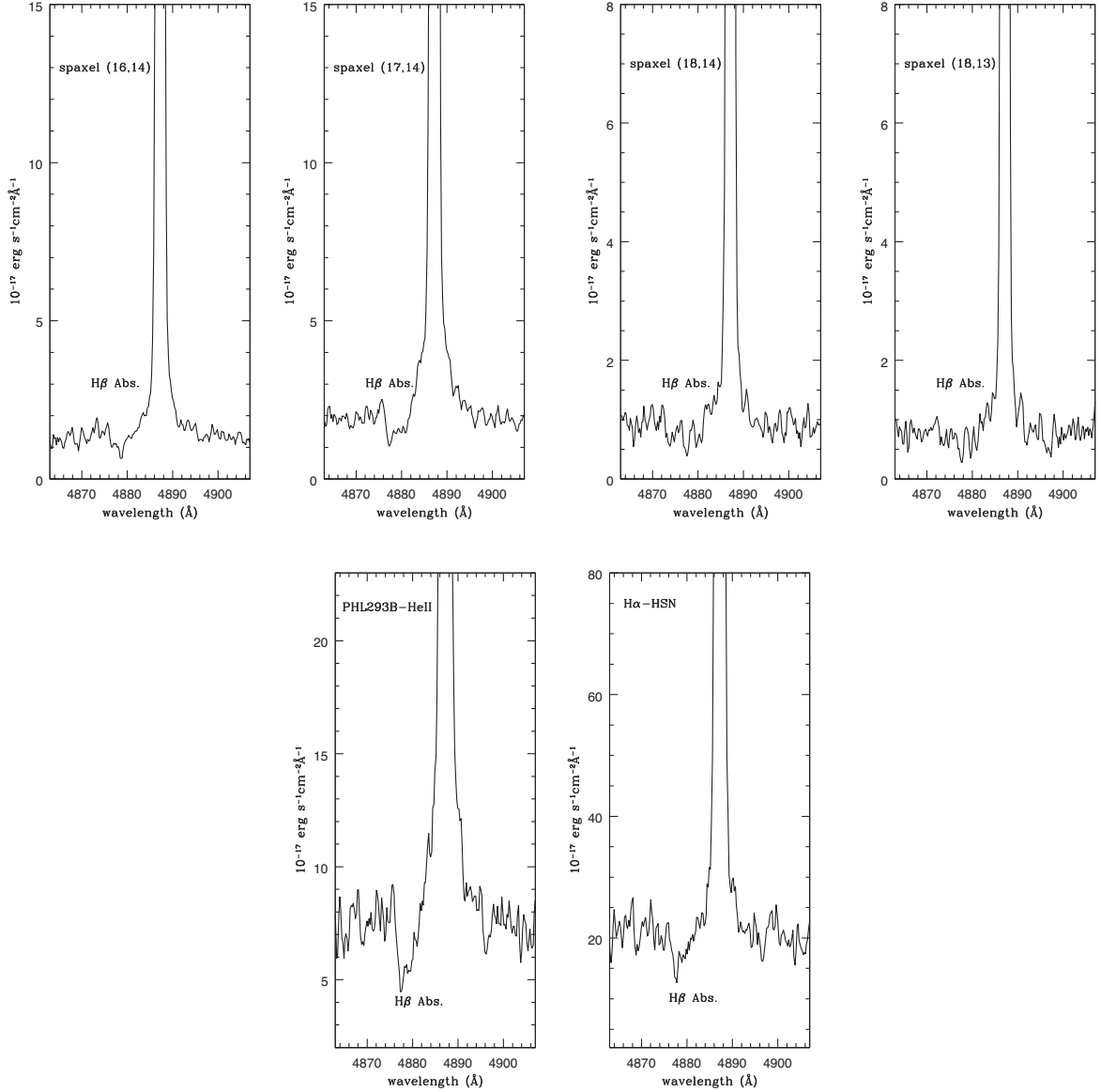


Figure 3. Spectral regions around $H\beta$ where we detect P Cygni-like profiles. The y-axis shows the flux in units of $10^{-17} \text{ erg s}^{-1} \text{ cm}^{-2} \text{ \AA}^{-1}$. Top row: the four individual spaxels marked with a black circle on the $H\beta$ broad emission map (see Fig. 2); for each spaxel we show in parenthesis the corresponding Cartesian coordinate (x,y) relative to the bottom left spaxel (0,0) in the maps. Bottom row: The spectra of the regions PHL 293B-He II and $H\alpha$ -HSN; the former is obtained by integrating the emission from all He II $\lambda 4686$ -emitting spaxels, while the latter corresponds to the sum of all spaxels with $H\alpha$ $S/N > 100$ (see Section 5 for details on the integrated spectra).

5 INTEGRATED SPECTRA ACROSS THE MEGARA FOV OF PHL 293B

Based on our IFU data, we integrated individual spectra of selected galaxy regions. We created for the first time the integrated spectrum of PHL 293B by adding the flux in all the spaxels with $H\alpha$ S/N (per spaxel) > 3 ; this matches an area of $\sim 194 \text{ arcsec}^2$ ($\sim 2.4 \text{ kpc}^2$) enclosing basically all the nebular emission across our FOV. In addition, by summing the emission from the spaxels with $H\alpha$ $S/N > 100$ ($\sim 11.5 \text{ arcsec}^2$), we simulate the spectrum of the brightest region of the galaxy (hereafter $H\alpha$ -HSN region⁴), and whose boundary is shown overplotted on the map of $H\alpha$ (see Fig. 2). Finally, we obtained the spectrum of the region that we name PHL 293B-He II. To do so we

have integrated all He II-emitting spaxels which covers $\sim 3.5 \text{ arcsec}^2$ (see the He II map in Fig. 2).

The 1D spectra mentioned above are presented in Fig. 9. We derive the fluxes of the emission lines and associated uncertainties for these spectra using the same method as for individual spaxels (see Section 3). We computed the logarithmic reddening coefficient, $C(H\beta)$, by performing a least-square fit to the ratio of the measured-to-theoretical Balmer decrements as a function of the Miller & Mathews (1972) galactic reddening law (see also Hägele et al. 2008). The uncertainty of the fit is adopted as the error in $C(H\beta)$. The narrow component of the four strongest Balmer emission lines ($H\alpha$, $H\beta$, $H\gamma$, $H\delta$) have been used. Intrinsic Balmer line ratios were taken from Osterbrock & Ferland (2006) assuming case B recombination with electron temperature $T_e = 2 \times 10^4 \text{ K}$: $(H\delta/H\beta)_{\text{theo}} = 0.26$, $(H\gamma/H\beta)_{\text{theo}} = 0.47$, $(H\alpha/H\beta)_{\text{theo}} = 2.75$. Some issues were found

⁴HSN from High Signal to Noise ratio.

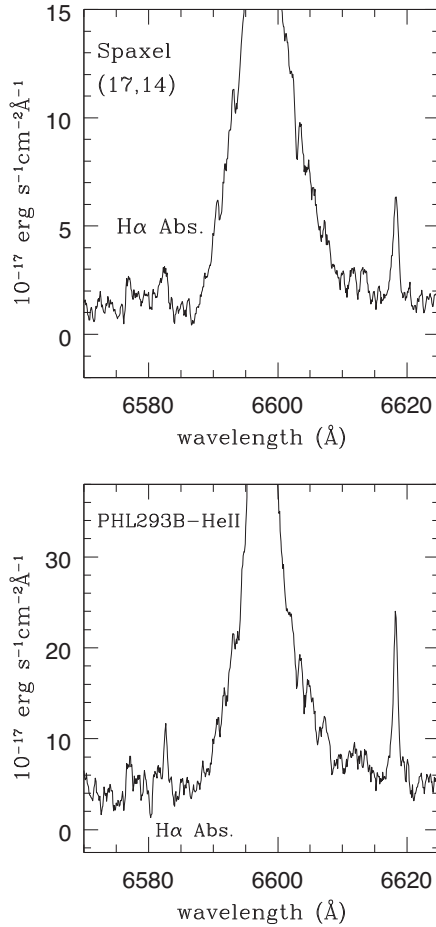


Figure 4. Spectral regions around H α showing hints for P Cygni-like profiles. The y-axis shows the flux in units of $10^{-17} \text{ erg s}^{-1} \text{ cm}^{-2} \text{ Å}^{-1}$. Top panel: spaxel (17,14) which corresponds to the H α peak marked with a plus (+) sign on all maps; Bottom panel: Spectrum of the PHL 293B-He II region as defined in the caption of Fig. 3 and in Section 5.

concerning the C(H β) computation. The blue grating covers the H δ and H γ , and the green spectra include both H γ and H β , while H α is measured in the red grating (see Section 2). We match the blue and green spectra by using the H γ line as reference which is measurable in both. We could not connect the green and red spectra since they share no lines. Thus, to minimize errors in the de-reddened ratios between a certain emission line and H β , we always take first its ratio in relation to the closest hydrogen emission line (i.e. H δ in the case of [O II] λ 3726, [O II] λ 3729 and [Ne III] λ 3868 λ ; H α in the case of [N II], HeI6678 and [S II]) and then we renormalize it using the corresponding theoretical Balmer ratio (e.g. Pérez-Montero et al. 2009, 2011; Kehrig et al. 2011).

Table 2 presents the relative fluxes of the de-reddened narrow emission lines measured from the integrated spectra; fluxes are normalized to the H β flux = 1000. We note that the values of C(H β) obtained here are in agreement with values derived for PHL 293B in the past (e.g. Izotov et al. 2012; Terlevich et al. 2014). Also, the listed H α /H β and H δ /H β ratios acceptably match their theoretical recombination values; the H γ /H β ratio shown in Table 2 makes use of the green-H γ flux, and is about 10 per cent–15 per cent smaller than the theoretical one. We verify that using the blue-H γ flux instead, the ratio between the de-reddened and theoretical H γ /H β lowers down to 3 per cent–5 per cent. The line ratios uncertainties

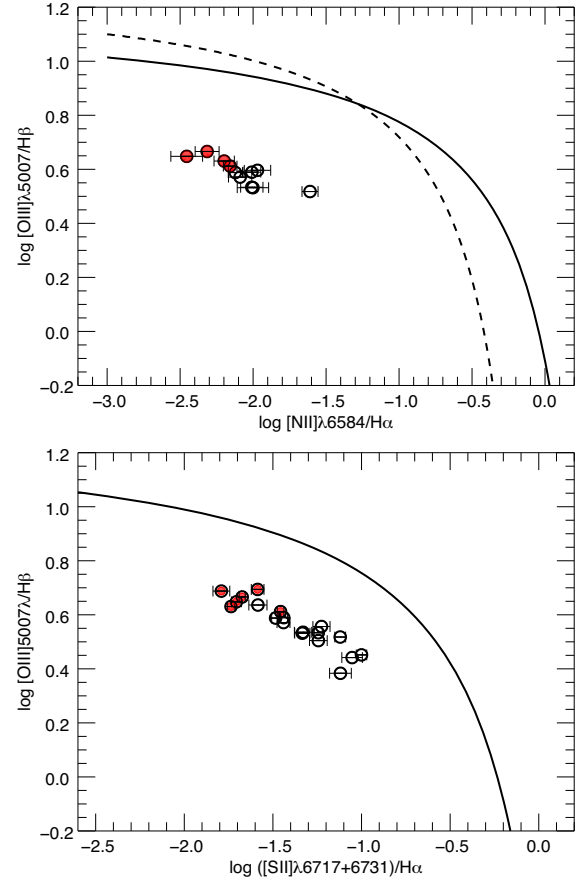


Figure 5. BPT diagnostic diagrams for PHL 293B. The open circles mark the individual spaxels from the data cube; red circles show the individual He II-emitting spaxels. The solid line (in the two panels) indicates the theoretical demarcation limit from Kewley et al. (2001) that separates objects where the gas ionization is mainly due to hot massive stars (below and to the left of the curve) from those where other ionizing mechanism is required. The dashed line in the [N II] λ 6584/H α plot (top panel) depicts the boundary between SF systems and AGNs from Kauffmann et al. (2003). Error bars in the y-axis are the same size or smaller than the symbols, and are not plotted for the sake of clarity.

consider error flux measurements and the error in C(H β), but do not take systematic uncertainties, e.g. due to the blue-green match. We note that the effects of these uncertainties on the line ratios upon which oxygen abundance and T_e [O III] estimates are based should be marginal since we obtain values in accord with other authors (see below). Since the [O II] lines are the most affected by extinction in our spectra, as a further check, we also corrected for reddening [O II] λ 3726, 3729/H β using only the green-H γ -to-H β ratio. We found that the variations in [O II] λ 3726, 3729/H β are within the quoted uncertainties in Table 2.

For our three selected galaxy regions (PHL 293B integrated, PHL 293B-He II, H α -HSN), we calculated physical properties and oxygen abundances as explained in Section 4 for single spaxel spectra. We calculated the nitrogen ionic abundance ratio, N^+/H^+ , from the PYNEB-based expression from Pérez-Montero (2017), using the [N II] λ 6584 emission line and assuming T_e [N II] \approx T_e [O II]; we derived the N/O ratio under the premise that $N/O = N^+/O^+$, based on the similitude of the ionization potentials of the ions N^+ and O^+ . Table 2 also lists the values of C(H β) and physical-chemical properties obtained for each spectrum region.

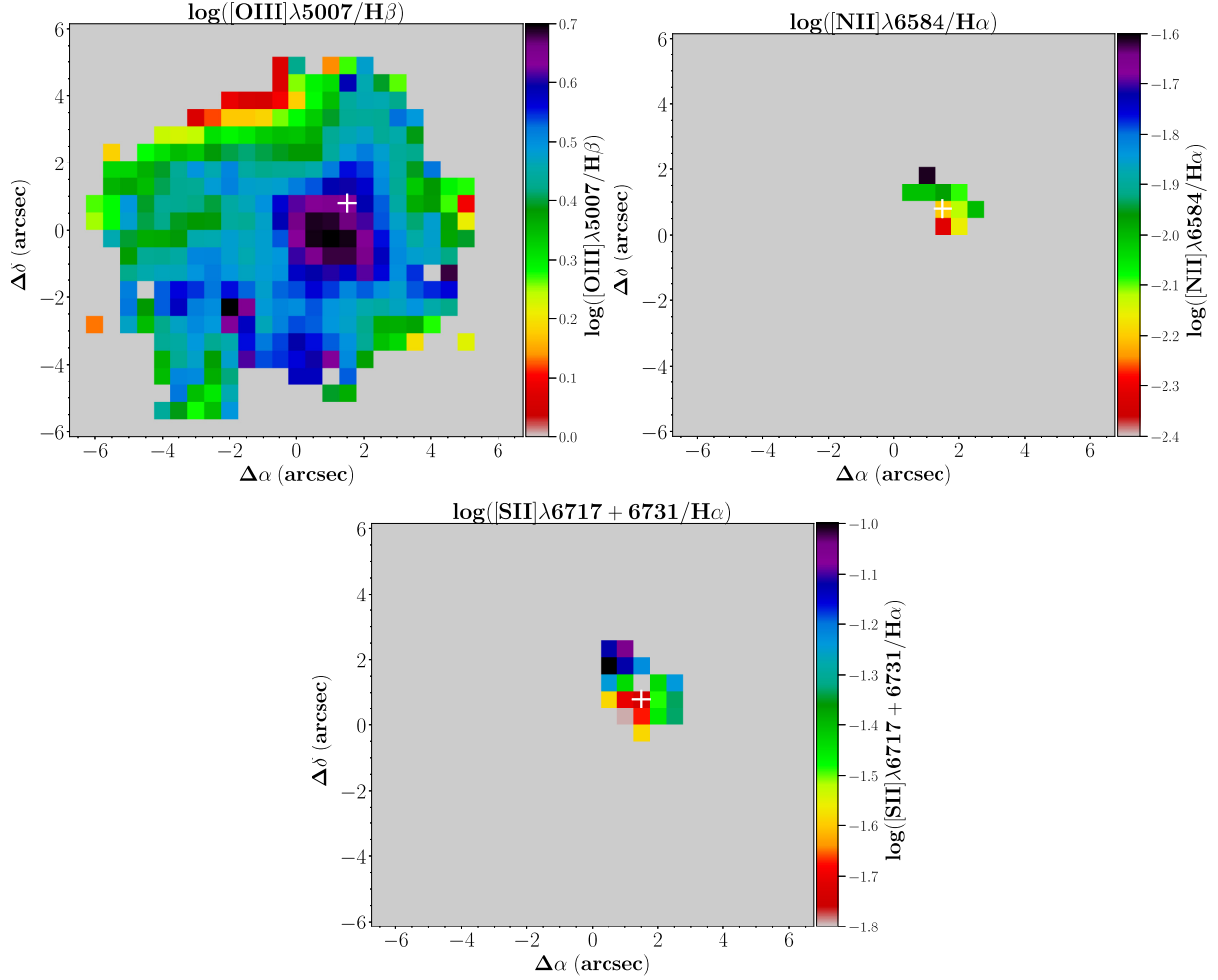


Figure 6. Maps of line ratios in logarithmic scale. East is left and North is up. The plus (+) sign is as indicated in Fig. 2.

By looking at Table 2 and Fig. 5, we find that the measurements of the integrated line-ratios $[\text{O III}]\lambda 5007/\text{H}\beta$, $[\text{N II}]\lambda 6584/\text{H}\alpha$, $[\text{S II}]\lambda 6717, 6731/\text{H}\alpha$ for the three selected regions are located below the demarcation lines in the BPT diagrams which implies an H II region-like ionization.

The comparison among the integrated electron temperature values from Table 2 shows similar $T_e[\text{O III}]$ considering the uncertainties. Concerning the oxygen abundances, we also find that the spectra of the regions PHL 293B-He II, H α -HSN, and PHL 293B-integrated yield equivalent values within the corresponding error bars. This is telling us that the metallicity obtained from the PHL 293B-integrated spectrum matches the O/H from the other two (physically smaller) selected zones. Therefore, according to our MEGARA data, the gas metallicity of PHL 293B is not only spatially homogenous (see previous section), but also independent of the aperture applied. Here, we take the O/H abundance of the integrated-spectrum $[12+\log(\text{O}/\text{H})=7.64 \pm 0.06 \sim 8$ per cent solar metallicity] as the representative metallicity of PHL 293B. This value is consistent, within the errors, with those reported in previous work (e.g. Kinman & Davidson 1981; Izotov et al. 2007; Papaderos et al. 2008; Guseva et al. 2009).

Regarding the nitrogen abundance, we find that the H α -HSN and PHL 293B-He II regions present similar N/O ratios within the uncertainties (see Table 2). The N/O values derived here are in agreement with the typical value of $\text{Log}(\text{N}/\text{O}) \approx -1.5$ to -1.6

characteristic for the plateau in the $12+\text{Log}(\text{O}/\text{H})$ versus $\text{Log}(\text{N}/\text{O})$ relation observed for low-metallicity systems (e.g. Garnett 1990; Thuan, Izotov & Lipovetsky 1995; Izotov & Thuan 1999; Mollá et al. 2006; van Zee & Haynes 2006; Pérez-Montero et al. 2011). Moreover, we confirm that the N/O ratios for these two regions match those obtained in earlier studies of PHL 293B (e.g. French 1980; Izotov et al. 2007).

In Table 3 we list the observed fluxes and dispersion of the broad and narrow emission components of H α and H β lines for the three integrated spectra described in this section. The origin of the broad emission and P Cygni-like features in the Balmer lines seen in the spectra of PHL 293B has been debated for many years. Discrepant scenarios involving a luminous blue variable star eruption, an expanding supershell or a stationary wind driven by a young cluster wind, and strongly radiative stationary cluster wind have been proposed (e.g. Izotov & Thuan 2009; Terlevich et al. 2014; Tenorio-Tagle et al. 2015). Burke et al. (2020) review the previous interpretations for the nature of PHL 293B including new 2019 Gemini data, and find a recent fading of broad H α emission (see also Allan et al. 2020); a broad to narrow H α flux ratio ($\text{H}\alpha$ B/N) of 0.41 from 2001 SDSS data and 0.10 from 2019 Gemini data are reported by Burke et al. (2020). Here we find $\text{H}\alpha$ B/N ~ 0.10 for all the three integrated regions indicating that the dissipation of the broad H α emission might have begun in 2017 when our observations were performed (see Table 3). However, while our

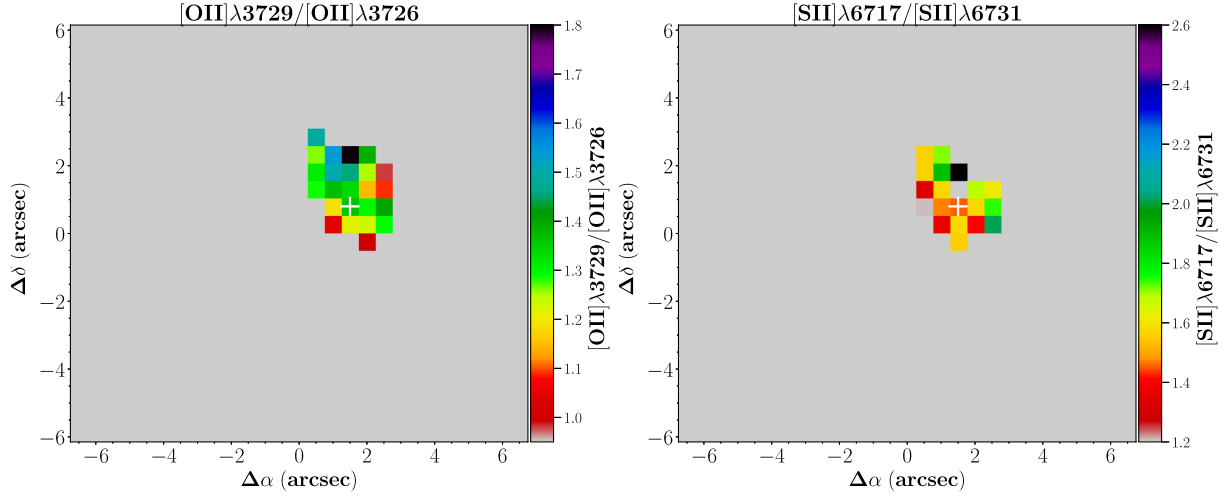


Figure 7. Indicators of nebula electron density. Maps for $[\text{O II}]\lambda 3729/[\text{O II}]\lambda 3726$ and $[\text{S II}]\lambda 6717/[\text{S II}]\lambda 6731$. East is left and North is up. The plus (+) sign is as indicated in Fig. 2.

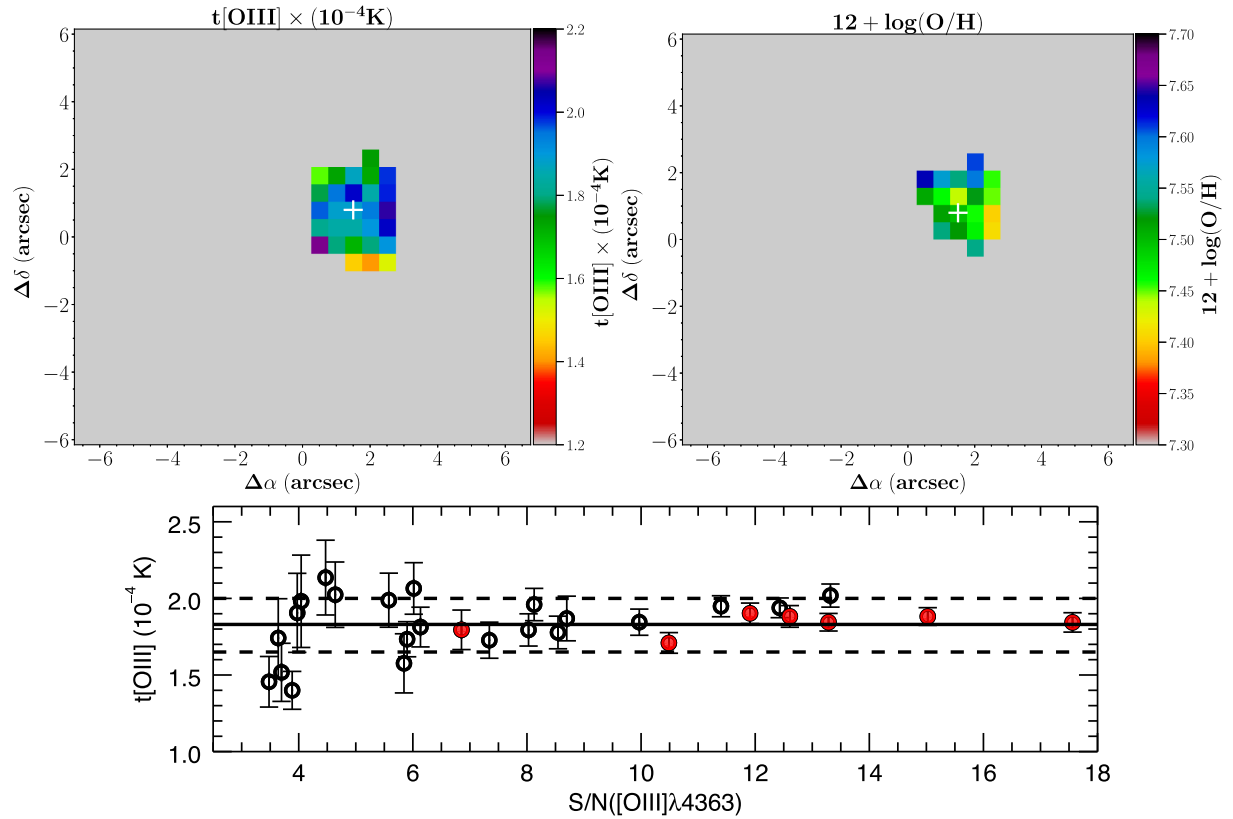


Figure 8. Top-left-hand panel: Map of the $[\text{O III}]\lambda 4363$ -derived $T_e[\text{O III}]$. Top-right-hand panel: Map of oxygen abundance derived only for spaxels with $T_e[\text{O III}]$ measurements available. The plus (+) sign is as indicated in Fig. 2. Bottom panel: $T_e[\text{O III}]$ versus the S/N of the $[\text{O III}]\lambda 4363$ line flux. The open circles represent individual spaxels; red circles indicate the seven $\text{He II}\lambda 4686$ -emitting spaxels; the solid horizontal line marks the mean value for $T_e[\text{O III}] \sim 1.83 \times 10^4$ K, while dotted lines represent $\pm 1\sigma$.

data reveal P Cygni-like features in $\text{H}\beta$ and $\text{H}\alpha$ (see Figs 3 and 4), P Cygni profile in $\text{H}\alpha$ is not visible in the 2019 Gemini spectra according to Burke et al. (2020).⁵ A long-lived Type II_n supernova (SN II_n) is proposed to be the most likely explanation

for the optical and spectral variability of PHL 293B by Burke et al. (2020). However, the lack of X-rays ($\lesssim 3 \times 10^{38} \text{ erg s}^{-1}$; e.g. Prestwich et al. 2013; Terlevich et al. 2014) in PHL 293B remains the big challenge to the SN II_n scenario. Larger time-scales spectroscopic follow-up should be necessary to clarify the variable spectral features of PHL 293B, but this is outside the scope of our study.

⁵Gemini spectra from Burke et al. (2020) cover from 5500–7500 Å.

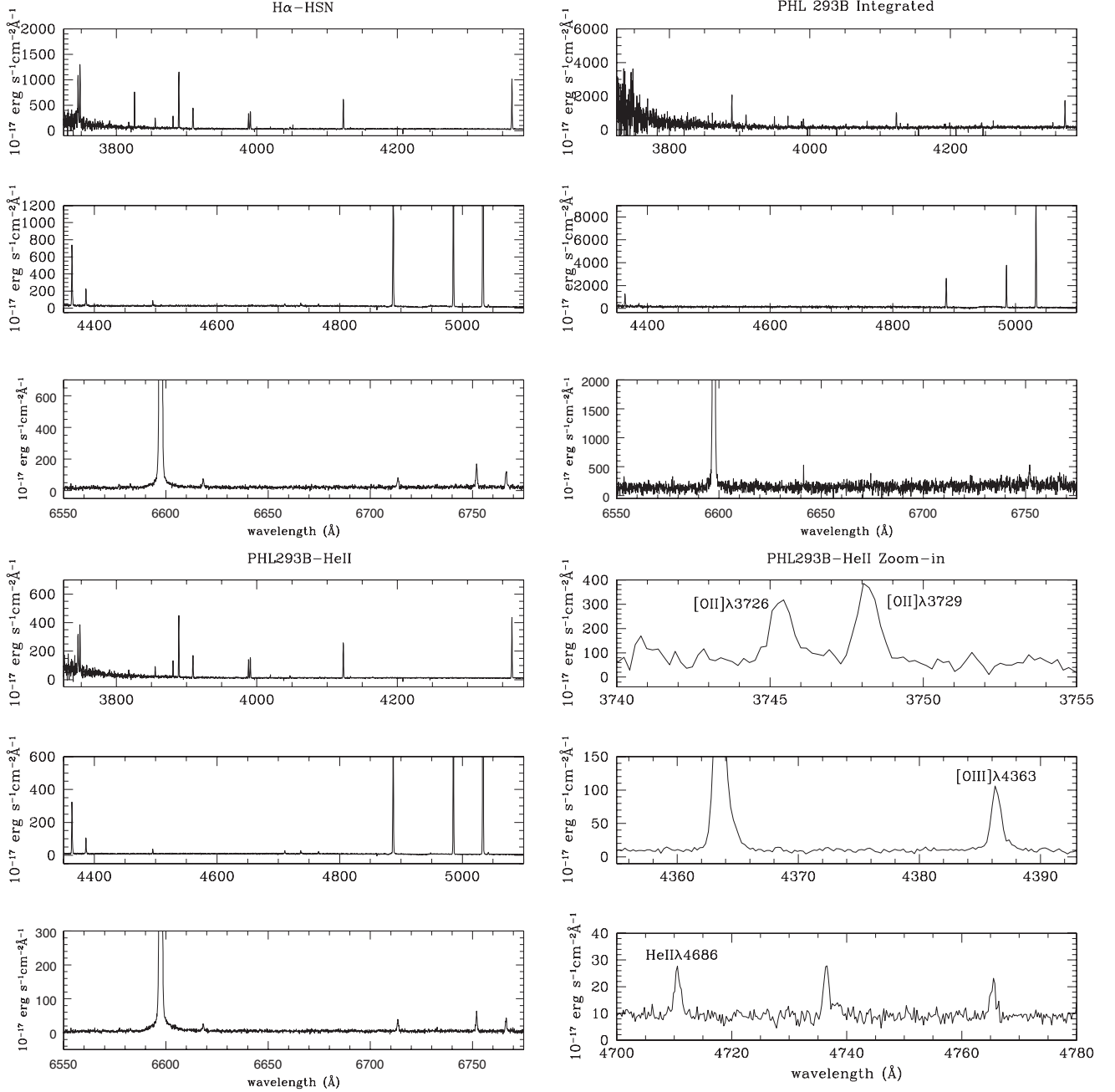


Figure 9. Flux-calibrated spectra of the three regions defined in Section 5. The y-axis shows the flux in units of $10^{-17} \text{ erg s}^{-1} \text{ cm}^{-2} \text{ Å}^{-1}$. Left-hand column, three first rows from top to bottom: the VPH405-LR, VPH480-LR, and VPH665-HR spectra for the H α -HSN region. Right-hand column, three first rows from top to bottom: the VPH405-LR, VPH480-LR, and VPH665-HR spectra for the PHL 293B-integrated region. Left-hand column, the three last rows from top to bottom: the VPH405-LR, VPH480-LR, and VPH665-HR spectra for the PHL 293B-He II region. For illustrative purposes, in the case of the PHL 293B-He II spectrum, the last three rows of the right-hand column display a zoomed-in view of the [O II] doublet, and of the wavelength ranges $\sim 4355\text{--}4390 \text{ Å}$ and $\sim 4700\text{--}4780 \text{ Å}$ showing the [O III] $\lambda 4363$ and nebular He II $\lambda 4686$ lines, respectively.

6 THE NEBULAR HE II $\lambda 4686$ IN PHL 293B

Photons with energy beyond 54 eV are needed to ionize He twice, so He II-emitting objects should host a relatively hard radiation field. While nebular He II emitters are atypical of nearby galaxies, they are expected to be usual at high- z ($z \gtrsim 6$) due to the predicted harder UV-ionizing spectra at the lower metallicities typical in the far-away Universe (e.g. Smith et al. 2015; Stark 2016; Stanway & Eldridge 2019). Next generation telescopes (e.g. JWST, ELT) are expected to detect the rest-frame UV of thousands of high-ionizing galaxies

in the reionization era. Therefore, studying the He II-ionization in metal-poor local objects is crucial to illuminate the properties of these reionization-epoch systems.

It is to be noted that the fraction of He II-emitting systems among metal-poor objects tend to be larger than that for higher metallicity galaxies observed in the local Universe (e.g. Kehrig et al. 2011; Shirazi & Brinchmann 2012). Ultra luminous X-ray binaries (ULXB), hot massive stars, and shocks are among the leading candidate sources discussed in the literature to explain the

Table 2. De-reddened narrow emission line-fluxes relative to $H\beta = 1000$ and physical properties from three selected regions^a.

| Wavelength (Å) | PHL 293B-Integrated ^b | Selected regions | |
|---|----------------------------------|---------------------------------|---------------------------------|
| | | H α -HSN ^c | PHL 293B-He II ^d |
| 3726 [O II] | 585 \pm 168 | 464 \pm 46 | 296 \pm 32 |
| 3729 [O II] | 760 \pm 118 | 544 \pm 42 | 340 \pm 27 |
| 3868 [Ne III] | 417 \pm 30 | 418 \pm 7 | 407 \pm 6 |
| 4100 H δ | 286 \pm 16 | 277 \pm 5 | 271 \pm 4 |
| 4340 H γ | 390 \pm 18 | 417 \pm 10 | 412 \pm 9 |
| 4363 [O III] | 84 \pm 14 | 106 \pm 6 | 113 \pm 5 |
| 4686 He II | – | 20 \pm 2 | 26 \pm 2 |
| 4714 [Ar IV] | – | 21 \pm 2 | 24 \pm 3 |
| 4740 [Ar IV] | – | 14 \pm 2 | 16 \pm 2 |
| 5007 [O III] | 3568 \pm 38 | 4068 \pm 44 | 4406 \pm 32 |
| 6563 H α (Narrow) | 2717 \pm 55 | 2831 \pm 39 | 2804 \pm 28 |
| 6584 [N II] | – | 20 \pm 3 | 16 \pm 4 |
| 6678 He I | – | 24 \pm 1 | 23 \pm 1 |
| 6717 [S II] | 82 \pm 10 | 54 \pm 2 | 36 \pm 1 |
| 6731 [S II] | – | 36 \pm 2 | 27 \pm 2 |
| c(H β) | 0.11 \pm 0.02 | 0.14 \pm 0.01 | 0.30 \pm 0.01 |
| F(H β) (erg s ^{−1} cm ^{−2}) | 4.28 \times 10 ^{−14} | 2.74 \times 10 ^{−14} | 1.86 \times 10 ^{−14} |
| F(He II) (erg s ^{−1} cm ^{−2}) | – | 5.41 \times 10 ^{−16} | 4.76 \times 10 ^{−16} |
| L(He II)(erg s ^{−1}) ^e | – | 3.45 \times 10 ³⁷ | 3.04 \times 10 ³⁷ |
| Q(He II)(photon s ^{−1}) ^f | – | 4.16 \times 10 ⁴⁹ | 3.66 \times 10 ⁴⁹ |
| log ([N II]6584/H α) | – | −2.16 | −2.25 |
| log ([S II]6717+6731/H α) | – | −1.50 | −1.66 |
| log ([O III]5007/H β) | 0.55 | 0.61 | 0.64 |
| T _e ([O III]) (K) | 16 335 \pm 1500 | 17 243 \pm 548 | 17 089 \pm 450 |
| T _e ([O II]) ^g (K) | 14 361 \pm 1080 | 15 015 \pm 394 | 14 904 \pm 324 |
| 12+log(O ⁺ /H ⁺) | 7.08 \pm 0.11 | 6.90 \pm 0.04 | 6.71 \pm 0.04 |
| 12+log(O ⁺⁺ /H ⁺) | 7.50 \pm 0.07 | 7.51 \pm 0.02 | 7.55 \pm 0.02 |
| 12+log(O/H) ^h | 7.64 \pm 0.06 | 7.60 \pm 0.02 | 7.61 \pm 0.02 |
| 12+log(N ⁺ /H ⁺) | – | 5.21 \pm 0.07 | 5.12 \pm 0.11 |
| log(N/O) | – | −1.68 \pm 0.08 | −1.59 \pm 0.11 |

Notes. (a) In all cases, the reddening correction for each line flux was performed relative to the closest Balmer recombination line (see the text for details)

(b) PHL 293B-integrated spectrum obtained by co-adding all spaxels with H α S/N > 3

(c) Spectrum created by adding all spaxels with H α S/N > 100

(d) Spectrum obtained by summing all He II-emitting spaxels

(e) He II luminosity at the distance of 23.1 Mpc

(f) Number of ionizing photons shortward of the He⁺ edge (see the text for details)

(g) $T_e[\text{O II}] = 0.72 \times T_e[\text{O III}] + 0.26$ (Pilyugin et al. 2006)

(h) $\text{O/H} = \text{O}^+/\text{H}^+ + \text{O}^{2+}/\text{H}^+$

nebular He II excitation in nearby SF galaxies (e.g. Garnett et al. 1991; Kehrig et al. 2011; Shirazi & Brinchmann 2012; Szécsi et al. 2015; Senchyna et al. 2020). However, despite observational and theoretical efforts, the origin of the He⁺ ionization is far to be a settled matter in several cases (e.g. Garnett et al. 1991; Kehrig et al. 2015, 2018; Kubátová et al. 2019; Plat et al. 2019; Zackrisson & Vikaus 2020). Current stellar models keep failing to reproduce the total emergent flux beyond 54 eV, specially in metal-poor galaxies (e.g. Kehrig et al. 2015, 2018; Stanway & Eldridge 2019).

The existence of narrow He II λ 4686 emission in PHL 293B has been noted before from long-slit spectroscopy (e.g. Izotov et al. 2007; Papaderos et al. 2008; Guseva et al. 2009; Izotov et al. 2011). Here, we produce the first He II λ 4686 spectral map of PHL 293B using MEGARA (see Fig. 2). From our data, we checked that the full width at half-maximum (FWHM) of the He II λ 4686 line matches that of other nebular emission lines like the strong [O III] λ 5007. The measured values of the mean and standard deviation for the FWHM(He II)/FWHM([O III] λ 5007) ratio are ~ 1.10 and 0.10,

respectively. The narrow line profile for the He II λ 4686 emission and its spatial extent are evidence of its nebular origin (see also Shirazi & Brinchmann 2012).

PHL 293B was observed with the *Chandra X-ray Observatory* on 2009 September for a total exposure time of 7.7 ks using the ACIS-S3 detector. There is no detection of X-ray emission up to an upper limit of $\sim 3 \times 10^{38}$ erg s^{−1} (Prestwich et al. 2013; Terlevich et al. 2014). This indicates that X-ray sources are unlikely to be the main responsible for the He II ionization in PHL 293B. On the other hand, the BPT line ratios measured both from the single He II-emitting spaxels and integrated spectra show values typical of H II region-like ionization (see Fig. 5 and Table 2) indicating hot massive stars as the dominant excitation source. This agrees with Burke et al. (2020) who claim that the narrow emission gas in PHL 293B is likely the H II region ionized primarily by stellar emission. Wolf–Rayet (WR) emission bumps are not detected in the spectra of PHL 293B. This means that different types of hot stars other than WRs should be contributing to the He II excitation. This

Table 3. Fit parameters of the broad and narrow hydrogen (H β , H α) emission lines for the regions listed in Table 2.

| Region ^a | Property | H β Narrow | H β Broad | H α Narrow | H α Broad |
|---------------------|--|------------------|-----------------|-------------------|------------------|
| PHL 293B-Integrated | Flux ^b | 3296 \pm 32 | – | 9720 \pm 61 | 1005 \pm 79 |
| | σ_{obs} (Å) ^c | 0.50 | – | 0.46 | 2.3 |
| | σ_{obs} (Km s ⁻¹) ^d | 31 | – | 21 | 105 |
| H α -HSN | Flux ^b | 1978 \pm 16 | 103 \pm 21 | 6203 \pm 15 | 589 \pm 31 |
| | σ_{obs} (Å) ^c | 0.49 | 2.22 | 0.46 | 3.17 |
| | σ_{obs} (Km s ⁻¹) ^d | 30 | 137 | 21 | 145 |
| PHL 293B-He II | Flux ^b | 933 \pm 5 | 65 \pm 9 | 3247 \pm 7 | 375 \pm 19 |
| | σ_{obs} (Å) ^c | 0.50 | 2 | 0.46 | 3.8 |
| | σ_{obs} (Km s ⁻¹) ^d | 31 | 123 | 21 | 174 |

Notes. (a) Regions as defined in Table 2.

(b) Observed fluxes in units of 10^{-17} erg s⁻¹ cm⁻².

(c) and (d) Observed σ (= FWHM/2.35) in units of Angstrom and Km s⁻¹, respectively

result agrees with the studies of the He II-emitting extremely metal-poor (XMP) galaxies IZw18 and SBS 0335-052E (see Kehrig et al. 2015, 2018). A detailed comparison of our observations to model predictions would be needed to constrain the hot ionizing stellar population in PHL 293B, but this exercise is beyond the scope of this paper.

For the PHL 293B-He II spectrum (obtained by adding all the He II-emitting spaxels; see Fig. 2 and Section 5), we computed the He II ionizing photon flux, $Q(\text{He II})_{\text{PHL 293B-He II}} = 3.66 \times 10^{49}$ photons s⁻¹ (see Table 2), from the corresponding reddening-corrected luminosity $L(\text{He II})$ using the relation $Q(\text{He II}) = L(\text{He II})/[j(\lambda 4686)/\alpha_B(\text{He II})]$ (assuming case B recombination, and $T_e([\text{O III}]) = 2 \times 10^4$ K; Osterbrock & Ferland 2006). Applying the same method for the H α -HSN region, whose area includes the PHL 293B-He II region (see Fig. 2 and Section 5 for details) we find that the H α -HSN region produces $Q(\text{He II}) = 4.16 \times 10^{49}$ photon s⁻¹ (see Table 2). This is ~ 14 per cent higher than $Q(\text{He II})_{\text{PHL 293B-He II}}$ which indicates that some small fraction of gas beyond the PHL 293B-He II region is also emitting He⁺-ionizing photons. The PHL 293B-He II and H α -HSN regions, together produce a total $Q(\text{He II}) = 7.82 \times 10^{49}$ photons s⁻¹ which can be taken as the He II ionizing budget measured for PHL 293B. It is worth noticing that the PHL 293B-integrated spectrum, created by summing almost all the emission across the MEGARA FOV, does not show the He II line (see Table 2). In this regard one should bear in mind that searches for reionization-era He II-emitters, for which only the total integrated spectra will be available, might be biased in the sense shown here, i.e. that a non-detection of the He II line does not necessarily mean the intrinsic absence of He II emission.

Using integral field spectroscopy (IFS), we also studied the spatial distribution of the nebular He II emission for the XMPs SBS 0335-052E and IZw18 (Kehrig et al. 2015, 2016, 2018). When comparing the observed $Q(\text{He II})$ for different regions across SBS 0335-052E and IZw18, we find, for both objects, that the highest absolute He II flux and maximum $Q(\text{He II})$ values correspond to the integrated spectrum of the galaxy, contrary to what we see in PHL 293B. This could suggest that the fraction of He II-ionizing hot stars, with respect to the total massive stellar content, should be higher in SBS 0335-052E and IZw18 in comparison to that of PHL 293B, and that a higher amount of He⁺-ionizing photons is reaching larger distances from the central star clusters in both SBS 0335-052E and IZw18. This might be related to the fact that, although the three objects are very low-Z, the specific star formation rate (sSFR) of SBS 0335-052E and IZw18 (170 and 166 Gyr⁻¹, respectively; Schneider, Hunt & Valiante 2016) is > 20 times that of PHL 293B sSFR ~ 6 Gyr⁻¹ (Filho et al. 2013).

Of course, higher statistics is necessary to make stronger statements on which properties can be dominant factors to determine the He II emitting nature of a galaxy.

All the results described above testify the importance of IFS for this kind of analysis, which allows us to collect all He II emission, and therefore deriving the absolute He II ionization budget.

7 SUMMARY AND CONCLUSIONS

We have analysed MEGARA observations of the nearby, very metal-deficient galaxy PHL 293B. This kind of objects constitute excellent laboratories for probing the conditions of galaxies in the early Universe. The data cover the optical wavelength range (~ 3700 – 6800 Å) within a field-of-view of $\sim 12.5 \times 11.3$ arcsec². MEGARA-IFU scans the entire spatial extent of the PHL 293B main body providing us with a new 2D view of the ionized ISM in this galaxy. Maps for the spatial distribution of relevant emission lines, line ratios, and physical-chemical properties for the ionized gas have been discussed. We were able to detect low intensity broad components and P Cygni-like profiles in the Balmer lines in agreement with previous work. We have checked that such components coincide spatially with the brightest star-forming cluster of the galaxy.

The BPT-line ratios ($[\text{O III}]\lambda 5007/\text{H } \beta$, $[\text{N II}]\lambda 6584/\text{H } \alpha$, $[\text{S II}]\lambda \lambda 6717, 6731/\text{H } \alpha$) measured both from individual spaxels and integrated spectrum regions agree with H II-like ionization. We measured the $[\text{O III}]\lambda 4363$ line flux over the central parts of the galaxy covering an area of ~ 0.12 kpc². For this zone, we measured O/H directly from the derived electron temperature $T_e[\text{O III}]$, and we find no significant variations in oxygen abundance; most of spaxels have $12+\log(\text{O}/\text{H})$ values spanning around ≈ 7.5 – 7.6 . For the first time, we derive the PHL 293B integrated spectrum by summing the spaxels with H α S/N > 3 . We take the O/H abundance of the PHL 293B integrated spectrum, $12+\log(\text{O}/\text{H}) = 7.64 \pm 0.06 \sim 8$ per cent solar metallicity, as the representative metallicity of the galaxy. Such value concurs with the ones on a spaxel-by-spaxel basis, and it also matches with those found in the literature.

Here, we derive the first spectral map for the nebular He II $\lambda 4686$ line and compute the He II ionization budget in PHL 293B. Our observations together with data from the literature indicate that neither Wolf-Rayet stars nor X-ray binaries are the main responsible for the He II ionization in PHL 293B. This is in the line of our studies on the two XMPs SBS 0335-052E and IZw18 based on IFS. Additional IFS studies of large samples of very metal-deficient and nebular He II-emitters are needed to better understand the nature of these objects.

ACKNOWLEDGEMENTS

Based on observations made with the Gran Telescopio Canarias (GTC), installed in the Spanish Observatorio del Roque de los Muchachos of the Instituto de Astrofísica de Canarias, in the island of La Palma. This work is (partly) based on data obtained with MEGARA instrument, funded by European Regional Development Funds (ERDF), through Programa Operativo Canarias FEDER 2014-2020. We thank the referee for a helpful report and thank M.A. Guerrero for useful discussion. We acknowledge financial support from the Spanish Ministry of Economy and Competitiveness under grant AYA2016-75808-R, which is partly funded by the European Regional Development Fund, and from the Excellence Network MagNet (AYA2017-90589-REDT). This work has been partially funded by research project AYA2016-79724-C4-4-P from the Spanish PNAYA. CK, JIP, JVM, SDP, and EPM acknowledge financial support from the State Agency for Research of the Spanish MCIU through the ‘Center of Excellence Severo Ochoa’ award to the Instituto de Astrofísica de Andalucía (SEV-2017-0709).

This work is based on observations collected with GTC at the Roque de los Muchachos Observatory.

DATA AVAILABILITY

The data underlying this article are part of the MEGARA commissioning observations and are available in the article.

REFERENCES

- Allan A. et al., 2020, *MNRAS*, 496, 1902
 Asplund M. et al., 2009, *ARA&A*, 47, 481
 Baldwin J. A., Phillips M. M., Terlevich R., 1981, *PASP*, 93, 5
 Burke C. J. et al., 2020, *ApJ*, 894, L5
 Cairós L. M. et al., 2001, *ApJS*, 136, 393
 Cairós L. M. et al., 2009, *A&A*, 507, 1291
 Cairós L. M. et al., 2010, *A&A*, 520, A90
 Carrasco E. et al., 2018, in Evans C. J., Simard L., Takami H., eds, *Proc. SPIE Conf. Ser. Vol. 10702, Ground-based and Airborne Instrumentation for Astronomy VII*. SPIE, Bellingham, p. 1070216
 Duarte Puertas S. et al., 2019, *A&A*, 629, A102
 Fernández V. et al., 2018, *MNRAS*, 478, 5301
 Filho M. E. et al., 2013, *A&A*, 558, A18
 French H. B., 1980, *ApJ*, 240, 41
 Garnett D. R., 1990, *ApJ*, 363, 142
 Garnett D. R. et al., 1991, *ApJ*, 373, 458
 Gil de Paz A. et al., 2018, in Evans C. J., Simard L., Takami H., eds, *Proc. SPIE Conf. Ser. Vol. 10702, Ground-based and Airborne Instrumentation for Astronomy VII*. SPIE, Bellingham, p. 1070217
 Guseva N. G. et al., 2009, *A&A*, 505, 63
 Guseva N. G. et al., 2017, *A&A*, 599, A65
 Hägele G. F. et al., 2008, *MNRAS*, 383, 209
 Izotov Y. I., Thuan T. X., 1999, *ApJ*, 511, 639
 Izotov Y. I., Thuan T. X., 2009, *ApJ*, 690, 1797
 Izotov Y. I. et al., 1999, *ApJ*, 527, 757
 Izotov Y. I., Chaffee F. H., Green R. F., 2001, *ApJ*, 562, 727
 Izotov Y. I. et al., 2004, *A&A*, 421, 539
 Izotov Y. I. et al., 2006a, *A&A*, 448, 955
 Izotov Y. I. et al., 2006b, *A&A*, 459, 71
 Izotov Y. I., Thuan T. X., Guseva N. G., 2007, *ApJ*, 671, 1297
 Izotov Y. I. et al., 2011, *A&A*, 533, A25
 Izotov Y. I., Thuan T. X., Guseva N. G., 2012, *A&A*, 546, A122
 Izotov Y. I. et al., 2018, *MNRAS*, 473, 1956
 Izotov Y. I., Thuan T. X., Guseva N. G., 2019, *MNRAS*, 483, 5491
 James B. L. et al., 2017, *MNRAS*, 465, 3977
 Kauffmann G. et al., 2003, *MNRAS*, 346, 1055
 Kehrig C., Telles E., Cuisinier F., 2004, *AJ*, 128, 1141
 Kehrig C. et al., 2006, *A&A*, 457, 477
 Kehrig C. et al., 2008, *A&A*, 477, 813
 Kehrig C. et al., 2011, *A&A*, 526, A128
 Kehrig C. et al., 2013, *MNRAS*, 432, 2731
 Kehrig C. et al., 2015, *ApJ*, 801, L28
 Kehrig C. et al., 2016, *MNRAS*, 459, 2992
 Kehrig C. et al., 2018, *MNRAS*, 480, 1081
 Kewley L. J. et al., 2001, *ApJ*, 556, 121
 Kinman T. D., Davidson K., 1981, *ApJ*, 243, 127
 Kobulnicky H. A., Skillman E. D., 1996, *ApJ*, 471, 211
 Kubátová B. et al., 2019, *A&A*, 623, A8
 Lehnert M. D., van Driel W., Le Tiran L., Di Matteo P., Haywood M., 2015, *A&A*, 577, A112
 López-Sanjuan C. et al., 2019, *A&A*, 631, A119
 Luridiana V., Morisset C., Shaw R. A., 2015, *A&A*, 573, A42
 Mainali R. et al., 2018, *MNRAS*, 479, 1180
 Markwardt C. B., 2009, *Astron. Data Analysis Softw. Syst. XVIII*, 411, 251
 Miller J. S., Mathews W. G., 1972, *ApJ*, 172, 593
 Mollá M. et al., 2006, *MNRAS*, 372, 1069
 Osterbrock D. E., Ferland G. J., 2006, *Astrophysics of Gaseous Nebulae and Active Galactic Nuclei*. University Science Books, CA
 Papaderos P. et al., 2006, *A&A*, 454, 119
 Papaderos P. et al., 2008, *A&A*, 491, 113
 Pascual S. et al., 2019, in Montesinos B., Asensio Ramos A., Buitrago F., Schödel R., Villaver E., Pérez-Hoyos S., Ordóñez-Etxeberria I., eds, *Highlights on Spanish Astrophysics X*, Salamanca, Spain, p. 227
 Pérez-Montero E., 2017, *PASP*, 129, 043001
 Pérez-Montero E. et al., 2009, *A&A*, 497, 53
 Pérez-Montero E. et al., 2011, *A&A*, 532, A141
 Pilyugin L. S. et al., 2006, *MNRAS*, 370, 1928
 Plat A. et al., 2019, *MNRAS*, 490, 978
 Prestwich A. H. et al., 2013, *ApJ*, 769, 92
 Sánchez S. F., 2020, *ARA&A*, 58, annurev
 Sánchez S. F. et al., 2012, *A&A*, 538, A8
 Schlafly E. F., Finkbeiner D. P., 2011, *ApJ*, 737, 103
 Schneider R., Hunt L., Valiante R., 2016, *MNRAS*, 457, 1842
 Senchyna P. et al., 2019, *MNRAS*, 488, 3492
 Senchyna P. et al., 2020, *MNRAS*, 494, 941
 Shirazi M., Brinchmann J., 2012, *MNRAS*, 421, 1043
 Smith A. et al., 2015, *MNRAS*, 449, 4336
 Sobral D. et al., 2019, *MNRAS*, 482, 2422
 Stanway E. R., Eldridge J. J., 2019, *A&A*, 621, A105
 Stark D. P., 2016, *ARA&A*, 54, 761
 Szécsi D. et al., 2015, *A&A*, 581, A15
 Tenorio-Tagle G. et al., 2015, *ApJ*, 800, 131
 Terlevich R. et al., 2014, *MNRAS*, 445, 1449
 Thuan T. X., Izotov Y. I., 2005, *ApJS*, 161, 240
 Thuan T. X., Izotov Y. I., Lipovetsky V. A., 1995, *ApJ*, 445, 108
 Thuan T. X., Izotov Y. I., Foltz C. B., 1999, *ApJ*, 525, 105
 Ucci G. et al., 2019, *MNRAS*, 483, 1295
 van Zee L., Haynes M. P., 2006, *ApJ*, 636, 214
 Westera P. et al., 2004, *A&A*, 423, 133
 Yan R. et al., 2016, *AJ*, 151, 8
 Zackrisson E., Vikaeus A., 2020, *IAUS*, 341, 187

This paper has been typeset from a \LaTeX file prepared by the author.